



MAY 01 2025

Dispersion and attenuation of guided waves in the Arctic Ocean with viscoelastic ice layer

Qitian Zeng ; Shengxing Liu; Liguang Tang ; Zhenglin Li; Wenyu Luo



J. Acoust. Soc. Am. 157, 3296–3309 (2025)

<https://doi.org/10.1121/10.0036568>



Articles You May Be Interested In

Theoretical and numerical study on transient acoustic wave propagation across ice layers in the Arctic Ocean

J. Acoust. Soc. Am. (May 2024)

Optical fiber infrasound sensor arrays: Signal detection and characterization capabilities in the presence of wind noise

J. Acoust. Soc. Am. (November 2007)

Stereoscopy of dust density waves under microgravity: Velocity distributions and phase-resolved single-particle analysis



Phys. Plasmas (March 2014)



LEARN MORE

Advance your science and career as a member of the
Acoustical Society of America

Dispersion and attenuation of guided waves in the Arctic Ocean with viscoelastic ice layer

Qitian Zeng,^{1,2}  Shengxing Liu,^{1,2,3,a)} Liguang Tang,^{1,4}  Zhenglin Li,^{2,3,5} and Wenyu Luo^{4,6}

¹College of Ocean and Earth Sciences, Xiamen University, Xiamen, 361102, China

²School of Ocean Engineering and Technology, Sun Yat-sen University, Zhuhai, 519000, China

³Southern Marine Science and Engineering Guangdong Laboratory (Zhuhai), Zhuhai, 519000, China

⁴State Key Laboratory of Acoustics, Institute of Acoustics, Chinese Academy of Sciences, Beijing, 100190, China

⁵Key Laboratory of Comprehensive Observation of Polar Environment (Sun Yat-sen University), Ministry of Education, 519000, China

⁶University of Chinese Academy of Sciences, Beijing, 100049, China

ABSTRACT:

The dispersion and attenuation characteristics of Arctic Ocean guided waves have significant applications in the analysis of under-ice acoustic fields and the inversion of acoustic parameters of ice, water, sediment, and seafloor. However, determining the complex dispersion relationship of guided waves propagating in a damped medium presents significant challenges. In this study, the Arctic Ocean was modeled as a viscoelastic ice–water–sediment–seafloor coupled system. Moreover, a spectral method was introduced to investigate the dispersion and attenuation of Arctic guided waves. The wave equations and boundary conditions were discretized, resulting in a generalized eigenvalue problem for guided waves propagating in this viscoelastic coupled system. A numerical program was then constructed to calculate the dispersion and attenuation curves of the guided waves. Furthermore, the influence of ice thickness, damping properties, and seawater depth on dispersion and attenuation was analyzed. The results obtained in this study provide theoretical guidance for Arctic Ocean acoustic detection, navigation, and trans-ice acoustic communication. © 2025 Acoustical Society of America. <https://doi.org/10.1121/10.0036568>

(Received 3 October 2024; revised 5 March 2025; accepted 14 April 2025; published online 1 May 2025)

[Editor: Timothy Duda]

Pages: 3296–3309

I. INTRODUCTION

As global climate change leads to the decline of ice and snow, the strategic military value of the Arctic is becoming increasingly evident, alongside its commercial exploitation and scientific research potential (Collins *et al.*, 2019; Chen *et al.*, 2021; Li *et al.*, 2021). Acoustic techniques are particularly important in seafloor exploration, resource exploitation, and environmental monitoring, as they are among the most effective means of transmitting information in marine environments. In recent years, the study of acoustic propagation characteristics in Arctic ice–water coupled systems has become a critical area of focus (Pelekanakis *et al.*, 2021; Ananiev *et al.*, 2022; Choi *et al.*, 2022), as it is foundational to many acoustic technologies used in the Arctic.

In our previous work, we investigated the transient propagation of guided waves across the ice layer in the Arctic Ocean (Zeng *et al.*, 2024), where the ice layer was modeled as a general elastic solid without damping, and the seafloor was modeled as a rigid interface. We also investigated the dispersion characteristics of guided waves in a more complex stratified Arctic Ocean system using the transfer matrix technique (Liu *et al.*, 2024), which considered the seafloor as a liquid sedimentary layer overlying a

rigid bottom. Moreover, theoretical and experimental studies of acoustic propagation in the Arctic Ocean have been conducted using methods, such as the normal mode theory, ray theory, and the wavenumber integral method (Lepage and Schmidt, 1994; Gavrilov and Mikhalevsky, 2006; Hope *et al.*, 2017; Baggeroer and Collis, 2022; Barclay *et al.*, 2023). However, there remains a gap in the study of guided-wave attenuation in the Arctic, as the complex dispersion within a damping medium has proven challenging to determine.

Most previous studies have assumed that the ice layer is a thin, plate-like elastic solid (Timco and Weeks, 2010), without considering its viscous damping effects. However, the acoustic properties of the Arctic ice layer and seafloor in real-world conditions are highly complex. For example, viscous damping parameters cannot be ignored, as they significantly influence the propagation of transverse waves (Wang and Shen, 2010; Li *et al.*, 2015; Cheng *et al.*, 2017; Åström and Benn, 2019; Zhang and Zhao, 2021). By considering wave attenuation (complex wave velocity), Collins (2015) generalized the parabolic equation method and rotated rational approximations (Milinazzo *et al.*, 1997) to an ocean environment with varying ice layer and sediment thicknesses. Furthermore, Collis *et al.* (2016) investigated the seismo-acoustic wave propagation in the ocean with ice layers, combining the normal mode method. The presence

^{a)}Email: liusx@xmu.edu.cn

of damping leads to complex characteristic equations, which shifts the numerical solving domain from a one-dimensional real axis to a two-dimensional complex plane. This makes traditional numerical methods, such as the bisection method (Liu *et al.*, 2024), ineffective, as the root-finding direction becomes indeterminate. Additionally, complex root-finding schemes, such as the Muller method (Muller, 1956), which rely on quadratic interpolation, often encounter difficulties in finding or solving roots because they assume that each computational grid in the complex plane contains at most one complex root. Another complex root-finding approach, the minimum peak method proposed by Lowe (1995), has been used for ultrasonic non-destructive evaluation of complicated structured media. The method involves first assuming that the medium is elastic and calculating the dispersion data using the traditional bisection method. Next, the acoustic parameters of the elastic system are replaced with those of the corresponding viscoelastic medium, and the slope-tracking method is used to locate the new data point that minimizes the modulus of the complex dispersion equation. This approach is then updated to reflect the complex dispersion data of the viscoelastic waveguide. The real and imaginary parts of the complex dispersion data represent the propagation and attenuation characteristics, respectively. Barshinger and Rose (2004) applied the minimum peak method to calculate the dispersion and attenuation curves of guided waves in hollow cylindrical pipes with damping materials and verified its reliability by comparing the numerical results with experimental measurements.

Although the minimum peak method can solve dispersion and attenuation curves in viscoelastic structures, its numerical implementation involves multiple complex procedures, including those of the traditional bisection method and iterative minimization of the modulus of the complex dispersion equation, resulting in a substantial amount of coding. Moreover, because of the complexities of the dispersion equations for large-scale multi-layer structured waveguides and the lack of proof regarding the convexity of their characteristic equations, the computational results obtained using the minimum peak method may not be globally optimal. Meanwhile, the KrakenC normal mode program, developed by Porter and Reiss (1984, 1985), also requires extensive coding due to its reliance on a combination of numerical methods, such as the finite difference method, Sturm sequence, and the Richardson extrapolation.

To address these challenges in determining the dispersion relationship, the spectral method (Shen *et al.*, 2011) offers an effective approach for solving complex roots as one of the weighted residual methods. This method provides several advantages, including high numerical accuracy, minimal coding requirements, and fast computational speed (Liu and Qu, 1998; Valle *et al.*, 1999). Moreover, the spectral method rarely encounters the issue of missing roots. It begins by using the roots of orthogonal polynomials as interpolation points to discretize the physical space, transforming the continuous partial differential equations into a matrix eigenvalue problem that can be solved. Since its introduction

to fluid dynamics computations in the 1970s, the spectral method has been applied to the study of seismic waves and the dispersion of small-scale elastic guided waves (Orszag, 1972; Fornberg, 1975; Carcione *et al.*, 2002; Karpfinger *et al.*, 2008a, 2008b, 2010), becoming the third major numerical technique for solving partial differential equations after the finite difference and finite element methods. A widely cited work on the application of spectral methods to guided-wave dispersion is that of Adamou and Craster (2004), who examined the dispersion and attenuation in two-dimensional circumferential in-plane motion and radial axisymmetric motion in elastic circular waveguides, and the attenuation of waves in multilayered and anisotropic damping media. However, there is limited research on the application of spectral methods to the dispersion and attenuation characteristics of guided waves in the Arctic Ocean. Compared to small-scale circular waveguides, the ice–water composite structures of the Arctic Ocean are much larger in scale, making the construction of generalized eigenvalues significantly more complex. Furthermore, the treatments of ice–water interfaces and seafloor boundary conditions are intricate. The numerical stability of large-scale models also poses a greater challenge compared to smaller-scale models, especially in the study of ocean waveguides, where modal confusion must be carefully avoided.

In this study, the Arctic Ocean was modeled as a viscoelastic ice–water–sediment–seafloor coupled system. The ice layer was treated as a viscoelastic solid, the seawater layer as a non-viscous fluid, and the seafloor as a composite structure consisting of a damped liquid sediment layer overlying a viscoelastic solid half-space. During the implementation of the spectral method, Chebyshev orthogonal polynomials were used as the interpolation basis to construct the Chebyshev–Gauss collocation points and differential matrices for the ice, seawater, and sediment layers. For the seafloor, the Laguerre–Gauss collocation points and differential matrix were constructed using Laguerre orthogonal polynomials. The wave equations and boundary conditions were discretized and incorporated into a generalized eigenvalue problem for the coupled system. A numerical program was then developed to solve this eigenvalue problem, enabling an analysis of the attenuation characteristics of guided waves in the viscoelastic coupled system.

II. GOVERNING EQUATIONS AND CONSTRAINTS

The Arctic Ocean is usually covered by an ice layer; therefore, from an acoustic point of view, it is composed of ice, seawater, sediment, and seafloor layers, as shown in Fig. 1. The xoz Cartesian coordinate system was used for this study. The roughness of both the ice–water interface and the seafloor was neglected. The ice layer was modeled as a viscoelastic solid with a thickness of h_1 , the seawater layer as a viscous fluid with a thickness of h_2 , and the bottom layer as a composite structure consisting of a viscous liquid sediment layer of thickness h_3 overlying a viscoelastic solid half-space seafloor.

The Lamé constants of the ice layer, seawater, sediment, and seafloor are denoted by λ_i and μ_i , ($i = 1, 2, 3, 4$), with the wave velocities in each layer given by the following equations:

$$c_{ip} = \sqrt{\frac{\lambda_i + 2\mu_i}{\rho_i}}, \quad c_{is} = \sqrt{\frac{\mu_i}{\rho_i}}. \quad (1)$$

It is important to note that only the first Lamé constant λ_i is applicable for liquid layers, as acoustic waves propagate as longitudinal motion in liquids. Therefore, $\mu_i = 0$, ($i = 2, 3$).

In elastic media, the Lamé constants are real. However, in an acoustic medium with damping, they become complex, resulting in complex acoustic velocities (Lowe, 1995; Barshinger and Rose, 2004), indicating acoustic propagation with attenuation. The dissipation factor δ and attenuation coefficient α are used to describe the damping effect quantitatively (Jensen *et al.*, 2011), and they relate to the acoustic velocity c as follows:

$$\alpha = 54.58\delta, \quad \text{Im}(c) = \delta \text{Re}(c). \quad (2)$$

The unit of the attenuation coefficient α is [dB/Λ], where Λ is the wavelength of the acoustic wave. The dissipation factor δ depicts the ratio between the real and imaginary parts of the complex acoustic velocity.

The longitudinal displacement potential ϕ_i , ($i = 1, 2, 3, 4$) and the transverse displacement potential ψ_i , ($i = 1, 4$) in each layer are expressed as follows (Eringen and Suhubi, 1975):

$$\phi_i = \Phi_i(z)e^{j(kx - \omega t)}, \quad (3)$$

$$\psi_i = \Psi_i(z)e^{j(kx - \omega t)}, \quad (4)$$

where Φ_i and Ψ_i are functions of depth z , $j = \sqrt{-1}$ is the imaginary unit, k and ω are the wavenumber along the x

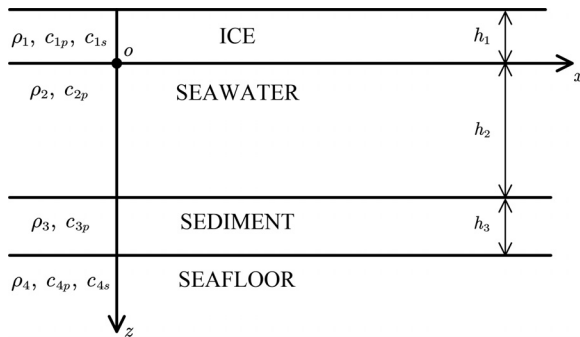


FIG. 1. Viscoelastic ice–water–sediment–seafloor coupled system for the Arctic Ocean. Thickness, density, and longitudinal and transverse wave velocities corresponding to ice layer are h_1 , ρ_1 , c_{1p} , and c_{1s} , respectively; thickness, density, and longitudinal wave velocity corresponding to seawater are h_2 , ρ_2 , and c_{2p} , respectively; thickness, density, and longitudinal wave velocity corresponding to sediment are h_3 , ρ_3 , and c_{3p} , respectively; and thickness, density, and longitudinal and transverse wave velocities corresponding to seafloor are h_4 , ρ_4 , c_{4p} , and c_{4s} , respectively. The origin of the coordinates is located at the boundary between the ice and seawater layers, representing the horizontal x direction and vertical z direction.

direction, and angular frequency, respectively. The longitudinal potentials $\Phi_i(z)$, ($i = 1, 2, 3, 4$) satisfy the Helmholtz equation as follows:

$$\left(\frac{d^2}{dz^2} - k^2\right)\Phi_i = -\frac{\omega^2}{c_{ip}^2}\Phi_i. \quad (5)$$

Transverse potentials $\Psi_i(z)$, ($i = 1, 4$) satisfy

$$\left(\frac{d^2}{dz^2} - k^2\right)\Psi_i = -\frac{\omega^2}{c_{is}^2}\Psi_i. \quad (6)$$

Equations (5) and (6) govern the acoustic waves in the ice–water–sediment–seafloor coupled system. However, they describe only the spatial distribution of the acoustic waves, while the coupled effects arise from the boundary conditions.

Let $\mathbf{u}_i = (u_i^x, u_i^z)$ and $\boldsymbol{\sigma}_i = (\sigma_i^{zz}, \sigma_i^{xz})$ denote the displacement and stress tensors in each layer. The boundary conditions are as follows: the upper surface of the ice layer is traction-free, the normal displacement and stress are continuous, and the shear stress is zero at the ice–water interface. Similarly, the normal displacement and stress are continuous at the water–sediment interface. In the interface between the sediment and the seafloor, the normal displacement and stress are continuous, and the shear stress in the viscoelastic seafloor is zero. In addition, the radiation condition is applied to the half-space seafloor, meaning that the potential functions at infinity are zero. These constraints can be formulated as follows:

$$\sigma_1^{zz}(x, -h_1) = 0, \quad \sigma_1^{xz}(x, -h_1) = 0, \quad (7)$$

$$u_1^z(x, 0) = u_2^z(x, 0), \quad \sigma_1^{zz}(x, 0) = \sigma_2^{zz}(x, 0), \quad (8)$$

$$\sigma_1^{xz}(x, 0) = 0,$$

$$u_2^z(x, h_2) = u_3^z(x, h_2), \quad \sigma_2^{zz}(x, h_2) = \sigma_3^{zz}(x, h_2), \quad (9)$$

$$\begin{aligned} u_3^z(x, h_2 + h_3) &= u_4^z(x, h_2 + h_3), \\ \sigma_3^{zz}(x, h_2 + h_3) &= \sigma_4^{zz}(x, h_2 + h_3), \\ \sigma_4^{xz}(x, h_2 + h_3) &= 0, \end{aligned} \quad (10)$$

$$\Phi_4(+\infty) = 0, \quad \Psi_4(+\infty) = 0. \quad (11)$$

During the implementation of the spectral method, the governing equations [Eqs. (5) and (6)] and the boundary constraints [Eqs. (7)–(11)] were discretized and formulated as a well-posed boundary eigenvalue problem. This problem was solved to obtain the dispersion and attenuation characteristics of guided waves in the coupled system, representing the nonlinear relationship between the angular frequency ω and wavenumber k .

III. SPECTRAL METHOD AND NUMERICAL PROCEDURES

The spectral method, a weighted residual method, is a global method used to solve differential equations. It offers several advantages, including arbitrary-order convergence with high accuracy, fewer code requirements, and the

capability to solve equations in complex domains (Adamou and Craster, 2004; Zharnikov *et al.*, 2013). These features are important for the numerical computation of large-scale models involving damping. The implementation of the spectral method involves discretizing the physical space to convert continuous differential equations into algebraic eigenvalue problems. Zeros of orthogonal polynomials, such as Jacobi, Chebyshev, Legendre, and Laguerre type polynomials, are used as interpolation points to generate computational grids (Hesthaven *et al.*, 2007; Shen *et al.*, 2011). These polynomial zeros are more densely distributed near the spatial boundaries, which helps avoid the Runge phenomenon (Epperson, 1987) compared to using equally spaced grids.

The objective of this study was to numerically determine the dispersion and attenuation of acoustic waves in the Arctic ice–water–sediment–seafloor coupled system described in Sec. II using the spectral method. By discretizing Eqs. (5) and (6) and applying the boundary conditions specified in Eqs. (7)–(11), a generalized eigenvalue problem was constructed and solved to obtain the dispersion and attenuation curves of guided waves in the coupled system.

A. Collocation point

In the finite physical spaces of the ice, seawater, and sediment layers, Chebyshev–Gauss collocation points were used, while in the half-space seafloor, Laguerre–Gauss collocation points were used.

Denoting N_i , ($i = 1, 2, 3$) as the number of collocation points in each layer, the Chebyshev–Gauss collocation points were generated using the following expression:

$$r_i^{l_i} = \cos \frac{(l_i - 1)\pi}{N_i - 1}, \quad l_i = 1, 2, \dots, N_i, \quad (12)$$

where the superscript and subscript of r represent the layer index and the collocation point index, respectively. As evident from Eq. (12), the value of the Chebyshev–Gauss collocation points decreases with increasing superscript, and all points are distributed within the interval $[-1, 1]$.

The Laguerre–Gauss collocation points are the zeros of the Laguerre polynomial. Denoting $\zeta_{l_4}^{N_4}$ as the first N_4 zeros of the Laguerre polynomial, the Laguerre–Gauss collocation points in the half-space seafloor are given by the following:

$$r_4^{l_4} = \zeta_{l_4}^{N_4}, \quad l_4 = 1, 2, \dots, N_4. \quad (13)$$

It should be noted that the zeros of the Laguerre polynomial are distributed within the interval $[0, \infty]$. Therefore, in practical calculations, the value of N_4 must be sufficiently large to effectively truncate the physical space for computational purposes.

B. Differential matrix

The differential matrix in the spectral method is used to approximate continuous derivative operations with discrete

algebraic operations. A function f is discretized into a vector \mathbf{f} at the collocation points, and its m -th order derivative can be calculated by multiplying \mathbf{f} with an m -th order differential matrix \mathbf{D}^m , as follows:

$$\mathbf{f}^{(m)} = \mathbf{D}^m \mathbf{f}. \quad (14)$$

The elements of the differential matrix depend on the choice of collocation points, and the construction and structure of the Chebyshev–Gauss differential matrix are presented in Appendix A. Further detailed explanations of the construction and derivation of the differential matrix can be found in the works of Shen *et al.* (2011), Trefethen (2000), Canuto *et al.* (2007), Fornberg (1998), Hesthaven *et al.*, 2007, and Funaro (2008).

The collocation points described in Sec. III A and the corresponding differential matrices must be transformed into a practical physical space (Adamou and Craster, 2004). The scaled collocation points and differential matrices are denoted by $z_i^{l_i}$ and \mathbf{D}_i^m , ($i = 1, 2, 3, 4$), respectively.

C. Construction of generalized eigenvalue problem

For a given wavenumber k , a generalized eigenvalue equation was constructed, in which the complex angular frequency ω serves as the eigenvalue. This scheme enables effective mode control of guided waves during the computational process.

Analytical solutions for motion in anisotropic or bending waveguides typically involve special functions, such as Hankel, Bessel, and Neumann functions, which can be challenging to compute accurately. One advantage of the spectral method is that it circumvents the need for these special functions, enhancing computational efficiency and numerical stability by converting continuous differential equations into discrete algebraic eigenvalue problems (Gridin *et al.*, 2003).

Using the collocation points and differential matrices, Eqs. (5) and (6) can be discretized as follows:

$$(\mathbf{D}_i^2 - k^2 \mathbf{I}_i) \Phi_i = -\frac{\omega^2}{c_{ip}^2} \Phi_i, \quad i = 1, 2, 3, 4, \quad (15)$$

and

$$(\mathbf{D}_i^2 - k^2 \mathbf{I}_i) \Psi_i = -\frac{\omega^2}{c_{is}^2} \Psi_i, \quad i = 1, 4, \quad (16)$$

respectively, where \mathbf{I}_i is an identity matrix of order N_i . Defining the matrix operator

$$\mathbf{L}_i = \mathbf{D}_i^2 - k^2 \mathbf{I}_i, \quad (17)$$

and the matrix function

$$\mathbf{M}_i(\theta) = \theta \mathbf{L}_i. \quad (18)$$

The discretized Eqs. (15) and (16) can then be integrated into a matrix form as follows:

$$\mathbf{L}\Theta = -\omega^2\mathbf{M}\Theta, \quad (19)$$

where the operator $\mathbf{L} = \text{diag}(\mathbf{L}_1, \mathbf{L}_1, \mathbf{L}_2, \mathbf{L}_3, \mathbf{L}_4, \mathbf{L}_4)$, the eigenvector $\Theta = (\Phi_1, \Psi_1, \Phi_2, \Phi_3, \Phi_4, \Psi_4)^T$, and the matrix function $\mathbf{M} = \text{diag}(\mathbf{M}_1(c_{1p}^{-2}), \mathbf{M}_1(c_{1s}^{-2}), \mathbf{M}_2(c_{2p}^{-2}), \mathbf{M}_3(c_{3p}^{-2}), \mathbf{M}_4(c_{4p}^{-2}), \mathbf{M}_4(c_{4s}^{-2}))$. The angular frequency ω is the eigenvalue.

The generalized eigenvalue problem described by Eq. (19) does not yet account for boundary constraints. The boundary conditions specified in Eqs. (7)–(11) must be discretized and embedded into Eq. (19) to formulate a well-posed boundary eigenvalue problem. The construction of this eigenvalue problem follows these steps.

First, discretized displacement and stress matrices, denoted as \mathbf{U} and \mathbf{S} , respectively, were constructed. The detailed construction procedures and expressions for each element are provided in Appendix B. Next, the corresponding rows of \mathbf{U} and \mathbf{S} were embedded into the generalized eigenvalue problem, i.e., Eq. (19), according to the boundary conditions outlined in Eqs. (7)–(11). The embedding regularities are shown in Appendix C. The boundary eigenvalue problem with embedded constraints is denoted as follows:

$$\tilde{\mathbf{L}}\Theta = -\omega^2\tilde{\mathbf{M}}\Theta. \quad (20)$$

The wavenumber k is implied as an internal parameter in operator $\tilde{\mathbf{L}}$. The real part of the complex eigenvalue ω describes the propagation characteristics of the guided waves, while the imaginary part reflects their attenuation characteristics.

D. Numerical procedures

Given a series of wavenumbers k , solving Eq. (20) for the eigenvalue ω yields the $\omega - k$ dispersion curves and attenuation curves of guided waves in the coupled system. The implementation steps are as follows:

- (1). Computation initialization: System acoustic parameters, such as density, acoustic velocity, thickness, and attenuation coefficient for each layer, were defined. The number of collocation points N_i , ($i = 1, 2, 3, 4$) was set. Furthermore, the corresponding collocation points and differential matrices were generated and scaled to match the actual physical spaces.
- (2). Solution of the generalized eigenvalue problem: For each given wavenumber, the discrete displacement and stress matrices \mathbf{U} and \mathbf{S} were constructed with embedded boundary conditions, as outlined in Appendices B and C. The complex eigenvalues ω were then obtained by solving the eigenvalue problem in Eq. (20).
- (3). Processing of numerical results: The number of eigenvalues obtained from solving Eq. (20) depends on the order of the eigenvalue problem, which corresponds to the order of the operator $\tilde{\mathbf{L}}$. Not all returned eigenvalues represent actual guided-wave modes; some are outliers

generated during discretization and numerical calculations that lack physical significance (Adamou and Craster, 2004). The outliers vary with the number of collocation points, while the eigenvalues corresponding to those propagating modes remain relatively stable. To eliminate outliers, the number of collocation points was adjusted and compared across several calculational operations. Moreover, at least two collocation points should be at each wavelength to ensure sufficiently high numerical accuracy according to the sampling theory, which states that the number of collocation points in each layer of the coupled system must satisfy the following:

$$N_i \geq \frac{2\pi f}{c_{ip}}, \quad (21)$$

where $f = \omega/2\pi$ is the frequency of the acoustic waves.

IV. NUMERICAL RESULTS AND DISCUSSIONS

In this study, a numerical program was developed using MATLAB (The MathWorks Inc., Natick, MA, R2024a) to calculate guided-wave dispersion and attenuation using the spectral method. Collocation points and differential matrices were generated using the subroutines provided by Weideman and Reddy (2000). The eigenvalue problem was solved using the built-in eig function of MATLAB, which is based on the QZ matrix factorization algorithm (Moler and Stewart, 1973).

The Arctic Ocean varies geographically and seasonally. Geographic influences are mainly characterized by differences in seawater depth at various locations, while seasonal influences are reflected in variations in ice layer thickness. Liu *et al.* (2021) investigated the influence of ice and seawater thicknesses on the phase- and group-velocity dispersion curves of guided waves in an elastic ice–water coupled system.

To verify the accuracy and efficiency of the spectral method, the dispersion curves of guided waves in an elastic ice–water system were calculated and compared with those obtained using the bisection method. Furthermore, the influences of ice and seawater layers on the propagation and attenuation of guided waves in a viscoelastic system were simulated and analyzed.

A. Dispersion of guided waves in elastic ice–water coupled system

In an elastic ice–water coupled system (Liu *et al.*, 2021), the ice is modeled as elastic, and the seafloor as rigid; thus, there is no dissipation within the ice or leakage from the seafloor.

According to Sturm–Liouville theory (Stakgold and Holst, 2011), all eigenvalues ω in this scenario are nonnegative real numbers. Moreover, the boundary conditions must be slightly adjusted. Specifically, Eqs. (10) and (11) are removed, while Eqs. (7) and (8) remain unchanged, and Eq. (9) is replaced by the following:

$$u_2^z(x, h_2) = 0, \quad (22)$$

which indicates a rigid seafloor boundary.

The acoustic parameters used in this computation were as follows: the depths of the elastic ice and seawater layers were 2 and 100 m, respectively; the densities of the ice and seawater were 917 and 1000 kg/m³, respectively; the longitudinal and transverse wave velocities in the ice were 3593.4 and 1809.8 m/s, respectively (McCammon and McDaniel, 1985); and the longitudinal wave velocity in seawater was 1500 m/s.

Figure 2 shows the first 10 orders of guided waves in the elastic ice–water coupled system. The red solid lines represent calculations obtained using the adaptive step-size bisection method developed by Liu *et al.* (2021), while the blue dotted lines represent calculations obtained using the spectral method developed in this study. The lowest curve corresponds to the first-order mode, with the second-, third-, and subsequent modes up to the tenth-order appearing progressively above it.

The bisection and spectral methods are two different numerical methods for calculating the dispersion relation. The former solves the potential functions satisfying the wave equation, obtains the analytical expression of the displacements and stresses, constructs the characteristic equation according to the boundary conditions, which is a determinant implicit function comprising the frequency ω and wavenumber k , and then solves it to obtain the system dispersion relationship. The latter method discretizes the wave equation directly, constructs a generalized eigenvalue equation to solve, and obtains the system dispersion relationship. The results from both methods show excellent agreement, demonstrating the validity of the spectral method.

Phase-velocity c_p and group-velocity c_g are given by the expression $c_p = \omega/k$ and $c_g = \partial\omega/\partial k$, respectively. Figure 3 shows the phase- and group-velocity curves for the first 10 orders of guided waves in the elastic ice–water

coupled system. A detailed analysis of the dispersion of guided waves in such a system in the Arctic Ocean was presented by Liu *et al.* (2021). In this section, we focus on the differences between the bisection and spectral methods.

Although both methods can be used to obtain the dispersion curves of guided waves in elastic systems, they approach the wave equation and boundary conditions in fundamentally distinct ways. Their computational efficiencies also vary significantly. The key differences between the two methods are as follows: (i) The bisection method searches for roots by progressively narrowing the interval in which the zeros of the dispersion equations are located. Each interval requires function evaluations at end points to determine the bisection strategy, meaning the subroutine for calculating the function value must be called frequently. This demands a high level of function continuity. In contrast, the spectral method converts the continuous differential operations into generalized eigenvalue problems in algebraic matrix form, which does not require high function continuity; (ii) the bisection method, even with adaptive step-size improvements, has high computational complexity. In the

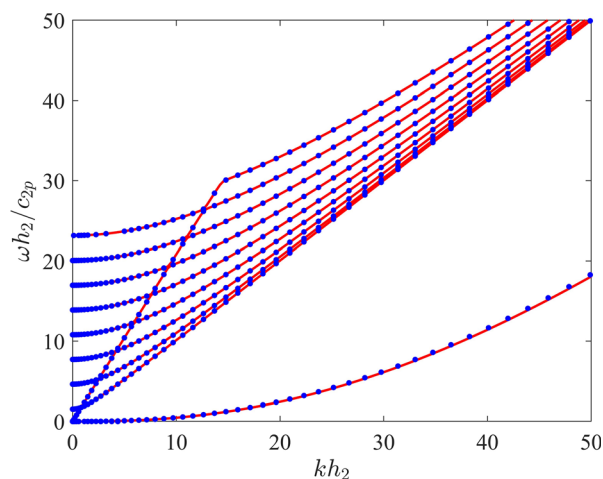


FIG. 2. $\omega - k$ relationship curves of the first 10 orders of guided waves in the elastic ice–water coupled system, where the red solid and blue dotted lines were calculated using the adaptive step-size bisection method developed by Liu *et al.* (2021) and spectral method, respectively.

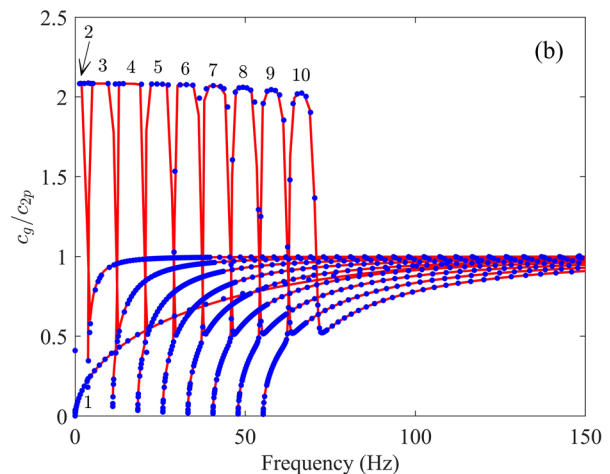
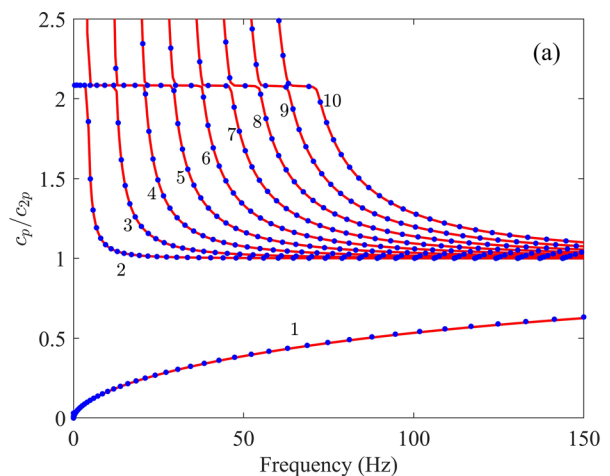


FIG. 3. (a) Phase- and (b) group-velocity curves of the first 10 orders of guided waves in the elastic ice–water coupled system. The red solid and blue dotted lines were calculated using the adaptive step-size bisection method developed by Liu *et al.* (2021) and spectral method, respectively. The numbers near the curves denote the mode order.

same computational environment (Intel Core i7-7700, 3.6 GHz, 16 GB RAM, Intel, Santa Clara, CA), the bisection method required 72 s to calculate the dispersion curves presented in Fig. 2, whereas the spectral method completed the task in 1.24 s; (iii) The time cost for the bisection method scales linearly with the order of the eigenvalue problem, while the spectral method scales cubically (Adamou and Craster, 2004), i.e., the time complexity is $O(N^3)$. This makes the spectral method more efficient for calculating low-order modes; and (iv) the spectral method has a wider application range than the bisection method. It can solve complex eigenvalue problems because the QZ algorithm used in the spectral method handles both real and complex numbers seamlessly (Moler and Stewart, 1973; Adamou and Craster, 2004). In contrast, the bisection method is limited to solving real eigenvalue problems.

B. Influence of thickness of viscoelastic ice layer

The thickness of the viscoelastic ice layer in the Arctic Ocean varies with geographic location, typically ranging from 2 to 6 m (Haas *et al.*, 2010; Hope *et al.*, 2017). Variations in ice thickness lead to changes in the dispersion curves of the guided waves in the system and affect the attenuation of these waves.

For the complex angular frequency ω , the phase-velocity is defined as follows:

$$c_p = \frac{\text{Re}(\omega)}{k}. \quad (23)$$

The attenuation, as defined by Sinha *et al.* (1992), is given as follows:

$$\gamma = \frac{\text{Im}(\omega)}{c_p}, \quad (24)$$

where the physical unit of attenuation γ is [Np/m]. When expressed in [dB/m], the transformation is as follows:

$$A = 20 \log_{10} e^\gamma. \quad (25)$$

The physical meaning of attenuation A is the propagation loss per unit propagation distance.

In the numerical simulations, the real parts of the longitudinal and transverse acoustic velocities in the viscoelastic ice layer were 3600 and 1800 m/s, respectively (Laible and Rajan, 1996). The density was 900 kg/m³ (Laible and Rajan, 1996), and the attenuation coefficients were $\alpha_{1p} = 0.216$ and $\alpha_{1s} = 0.648$ dB/Λ (McCammon and McDaniel, 1985; Rajan *et al.*, 1993), respectively. The seawater layer was modeled as a non-viscous fluid with a density of 1000 kg/m³, and a longitudinal acoustic velocity of 1500 m/s. The fluid sediment layer had a depth of 2 m, a density of 1500 kg/m³, a longitudinal acoustic velocity of 1550 m/s, and an attenuation coefficient $\alpha_{3p} = 0.2$ dB/Λ (Jensen *et al.*, 2011). The seafloor was modeled as a viscoelastic solid half-space with a density of 2900 kg/m³, longitudinal and transverse acoustic

velocities of 2200 and 1500 m/s, respectively, and corresponding attenuation coefficients α_{4p} and α_{4s} both of 0.5 dB/Λ (Jokat *et al.*, 1995).

The seawater depth was set to 100 m, and the ice layer depths were varied at 2, 4, and 6 m, respectively. Figure 4 shows the phase-velocity dispersion curves for the first 10 orders of guided waves. The longitudinal acoustic velocity c_{2p} of the seawater layer was used to normalize the phase-velocity. The black, red, and blue lines correspond to the phase-velocity curves of guided waves in the coupled system with ice layer depths of 2, 4, and 6 m, respectively. The bottom lines represent the first-order modes, while the curves progressing from left to right represent the second-through tenth-order modes.

Figure 4 indicates that ice thickness has a significant influence on the phase-velocity dispersion curve of the first-order mode. As the frequency increases, the phase-velocities of the first-order mode for ice layer depths of 2, 4, and 6 m converge to approximately $0.8 c_{2p}$, $0.76 c_{2p}$, and $0.63 c_{2p}$, respectively. Moreover, the phase-velocity curves of higher-order modes (the second order and above) exhibit minimal variation and display a ladder-like structure at approximately $2.1 c_{2p}$. These findings align with the results reported by Liu *et al.* (2021).

The attenuation of the guided waves is determined by the imaginary part of the angular frequency ω and phase-velocity c_p . Figure 5 shows the attenuation curves calculated using Eqs. (24) and (25) for the first 10 orders of guided waves in the 0–1100 Hz range, presented in three panels as the low-, middle-, and high-frequency bands. The black, red, and blue lines correspond to ice layer depths of 2, 4, and 6 m, respectively. The numbers near the curves denote the order of the guided-wave mode.

Figure 5 shows that, although the attenuation coefficient α in the waveguide is small, it still leads to significant guided-wave attenuation. As shown in Fig. 5(a), the attenuation of the first-order mode increases rapidly and monotonically with frequency and is considerably larger than those of

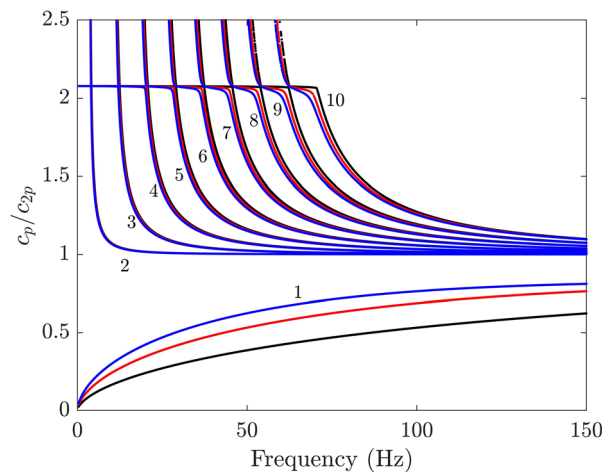


FIG. 4. Phase-velocity curves of the first 10 orders of guided waves in the coupled system, where the black, red, and blue lines correspond to ice layers with depths of 2, 4, and 6 m, respectively. The numbers near the curves denote the mode order.

the higher-order modes. The curves for the higher-order modes (the second order and above) display a fluctuating pattern, with each mode exhibiting a corresponding attenuation peak that shifts to a higher frequency as the mode order increases. Moreover, higher-order modes tend to have larger attenuation peak values. In addition, the thickness of the ice layer influences the attenuation of the guided waves. When the ice layer is thicker, the attenuation of the first-order mode decreases significantly, and the attenuation of the higher-order modes decreases only slightly. In the 100–500 Hz range, each mode presents a sub-peak, where higher orders exhibit higher sub-peak values, as shown in Fig. 5(b). Moreover, thicker ice layers result in a narrower frequency band for the sub-peaks. At frequency bands of 300–500 Hz, the attenuation curves tend to flatten. Furthermore, in the high-frequency band, i.e., the 500–1100 Hz band shown in Fig. 5(c), the attenuation of each mode decreases monotonically, with slight differences in the values.

The larger attenuation of the first-order mode, compared to the higher-order modes, supports the Liu *et al.* (2021) argument that the first-order mode in the ice–water coupled system is mainly influenced by the ice layer, whereas the higher-order modes result from the coupling between the ice and seawater layers.

Figure 5 also shows that guided-wave attenuation in the coupled system exhibits frequency-selective characteristics, concentrated mainly in the low-frequency band. As the frequency increases, the attenuation of the higher-order modes tends to stabilize.

C. Influence of damping of viscoelastic ice layer

The acoustic properties of the ice layer vary depending on geographic locations and environmental factors (Schwarz and Weeks, 1977; Alexander *et al.*, 2016; Hope *et al.*, 2017). In this study, we focus on the effect of ice damping properties on the attenuation curves of guided waves in the coupled system.

Rajan *et al.* (1993) reported that the compression wave attenuation within the ice layer typically ranges from 0.06 to 0.282 dB/m/kHz, which corresponds to 0.216 to 1.1015 dB/Λ. A commonly observed ratio between the shear wave attenuation coefficient α_s and the compression wave attenuation coefficient α_p is $\alpha_s = 3\alpha_p$ (McCammon and McDaniel, 1985). In the numerical simulation, the ice layer thickness was set to 8 m, and the attenuation coefficients of the longitudinal wave were set to 0.3, 0.5, and 0.7 dB/Λ, respectively. The attenuation coefficients of the transverse wave were set to three times the corresponding

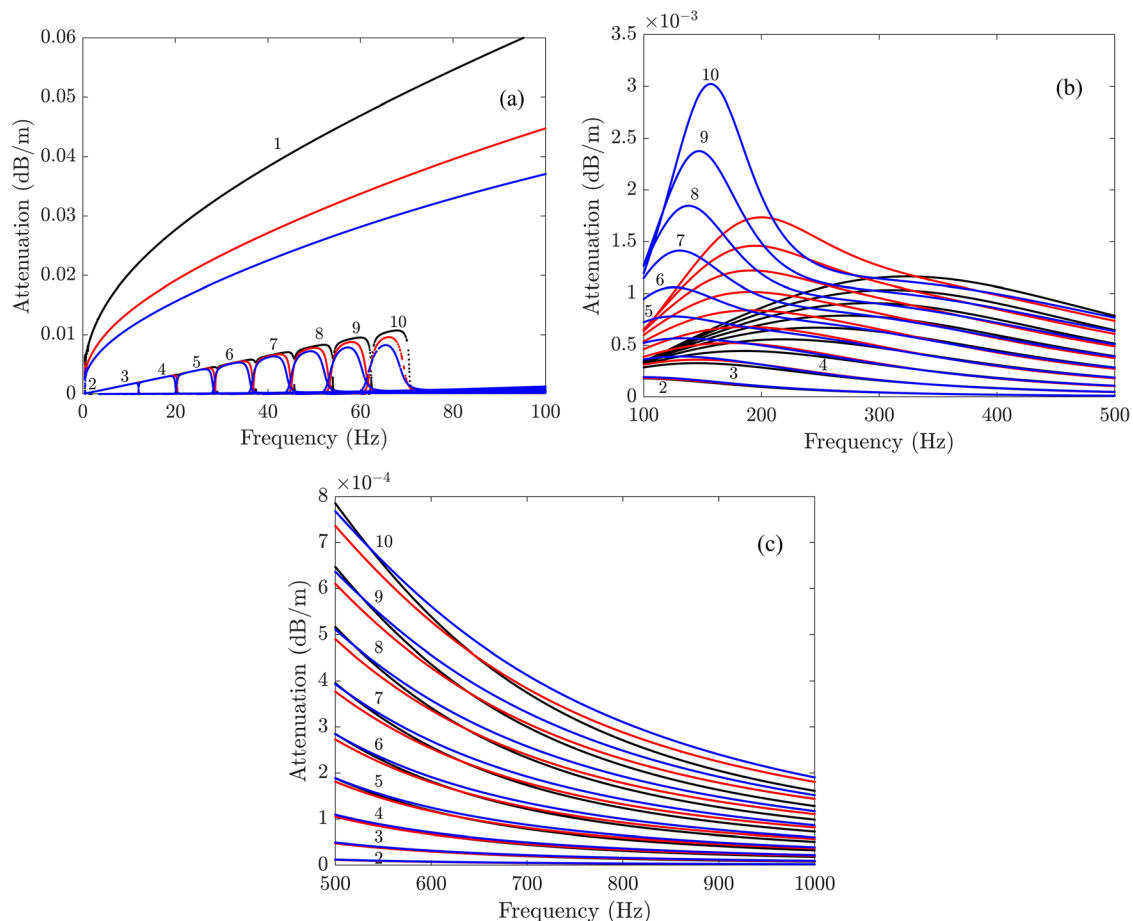


FIG. 5. Attenuation curves of the first 10 orders of guided waves in the coupled system, where the black, red, and blue lines correspond to ice layers with depths of 2, 4, and 6 m, respectively. The numbers near the curves denote the mode order. The three panels correspond to the (a) low-frequency band (0–100 Hz), (b) middle-frequency band (100–500 Hz), and (c) high-frequency band (500–1100 Hz), respectively.

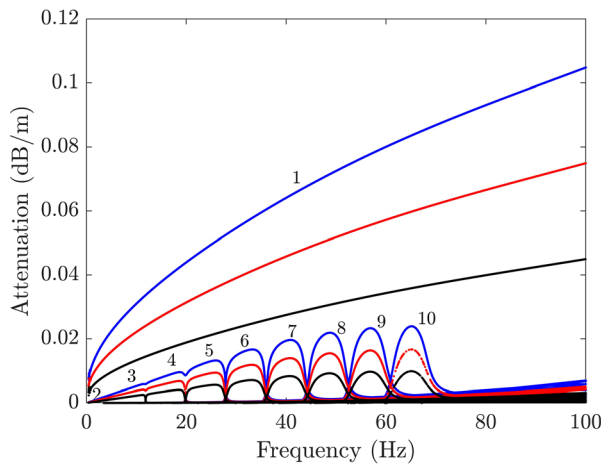


FIG. 6. Attenuation curves of the first 10 orders of guided waves in the coupled system, when attenuation coefficients of longitudinal wave were set to 0.3 (black lines), 0.5 (red lines), and 0.7 dB/Λ (blue lines), and attenuation coefficients of transversal wave were set to three times corresponding longitudinal wave. The numbers near the curves denote the mode order.

longitudinal wave values. All other parameters remained the same as those described in Sec. IV B.

Figure 6 presents the attenuation curves for the first 10 orders of guided waves in the ice–water–sediment–seafloor

coupled system with different ice damping properties. The black, red, and blue lines correspond to longitudinal wave attenuation coefficients of 0.3, 0.5, and 0.7 dB/Λ, respectively. A comparison between Figs. 5 and 6 reveals that the effect of ice damping properties on the attenuation curves of guided waves is more significant than the effect of ice thickness. As the attenuation coefficient increases, the propagation attenuation for all modes also increases. This is because the primary source of attenuation in the coupled system is the damping from the ice layer, with significantly less contribution from the spreading loss in the half-space seafloor. Furthermore, it is clear that the first-order mode is the most affected by changes in damping, showing a substantial increase in attenuation as the frequency rises.

D. Influence of depth of seawater layer

In addition to geographic and seasonal variations in ice thickness and acoustic properties, significant differences in seawater depth exist across various regions of the Arctic Ocean. These variations inevitably affect the dispersion characteristics of guided waves, such as the phase- and group-velocity curves (Liu *et al.*, 2021), and their propagation attenuation.

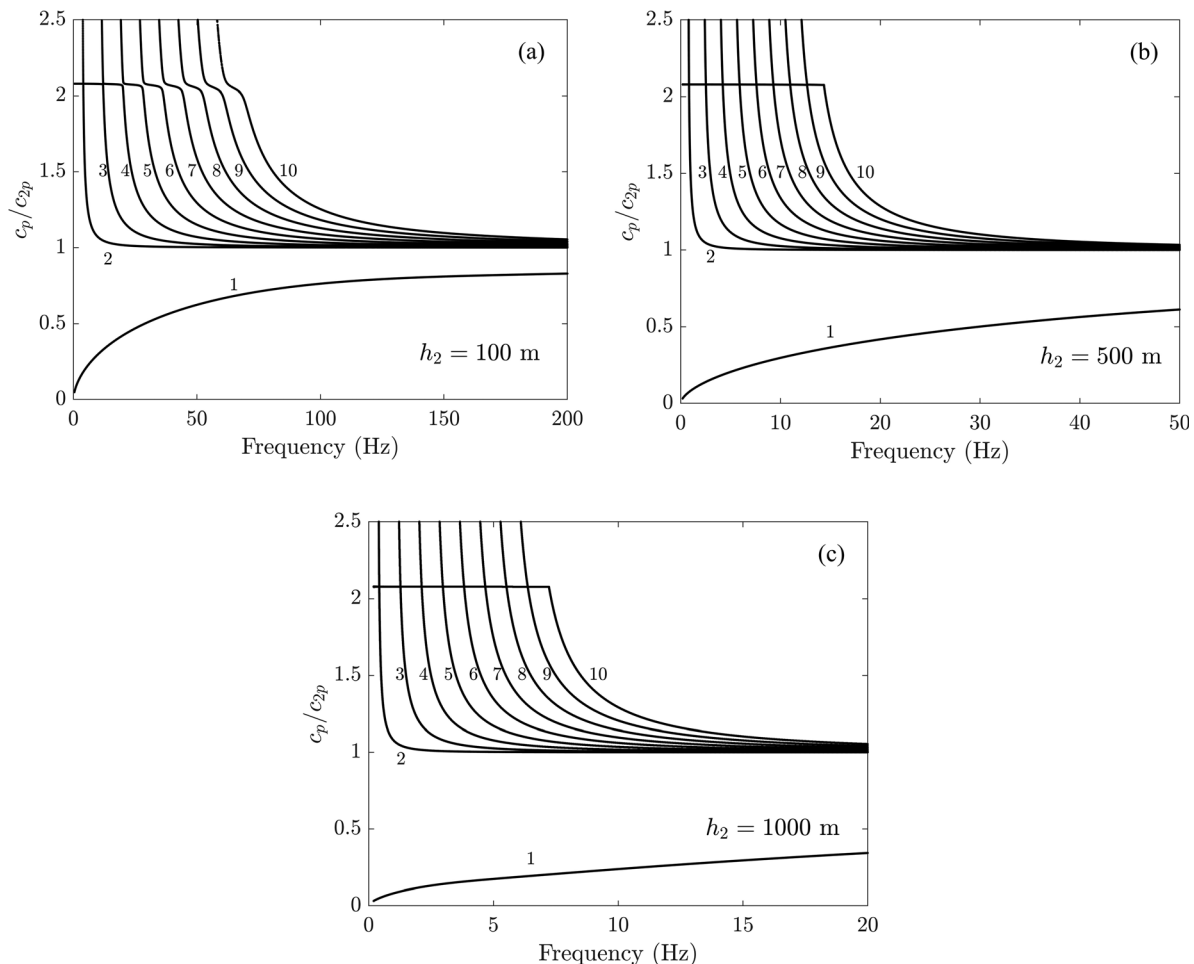


FIG. 7. Phase-velocity dispersion curves of the first 10 orders of guided waves in the coupled system. The seawater depths are 100 m (a), 500 m (b), and 1000 m (c), respectively. The numbers near the curves denote the order index.

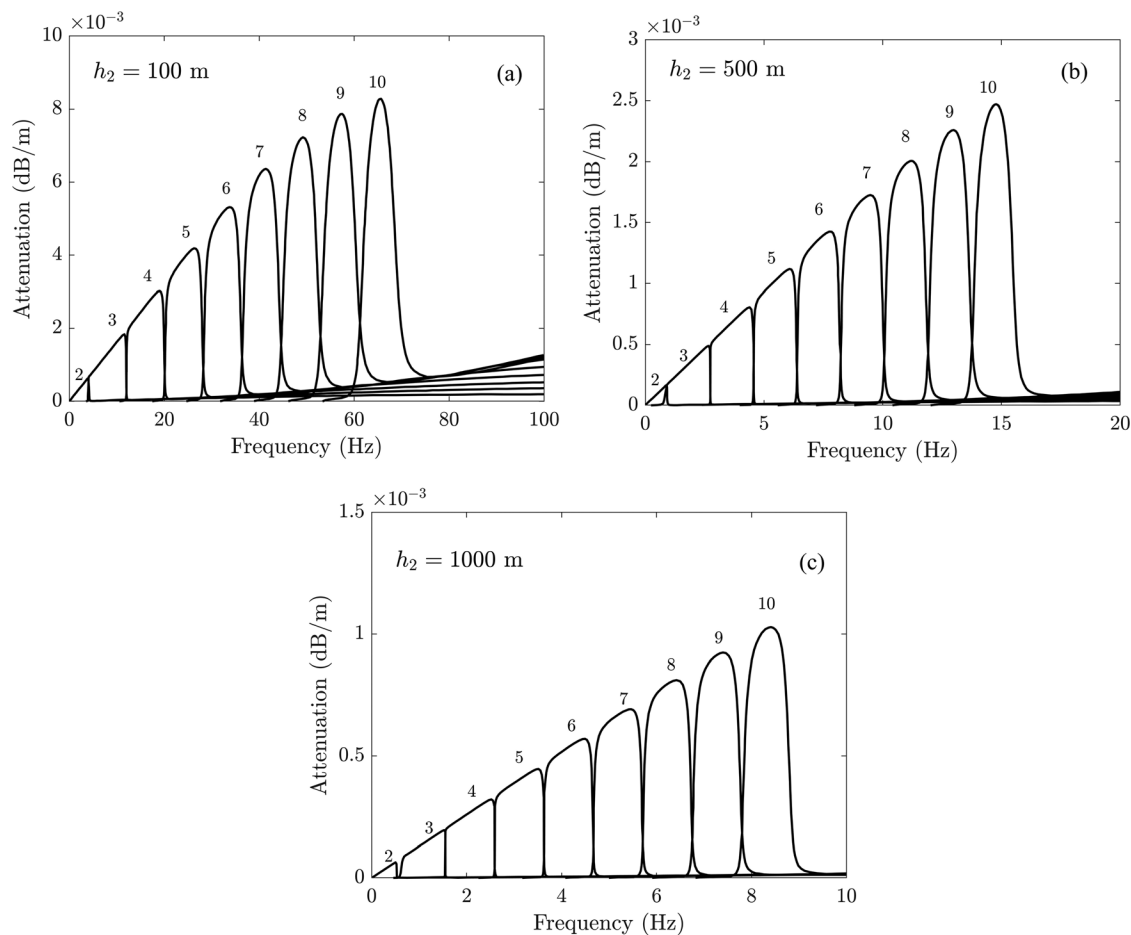


FIG. 8. Attenuation curves of higher-order modes 2–10 of the guided waves in the coupled system. The seawater depths are 100 m (a), 500 m (b), and 1000 m (c), respectively. The numbers near the curves denote the order index.

Figure 7 presents the phase-velocity dispersion curves for guided waves in the coupled system with an ice layer depth of 6 m and seawater depths of 100, 500, and 1000 m, respectively. The figure shows that, as the seawater depth increases, the strong dispersion region of the dispersion curve for the i -th ($i > 1$) guided-wave mode shifts toward lower frequencies. In addition, the thicker the seawater layer, the lower the cutoff frequency for the i -th ($i > 1$) guided-wave mode. The phase velocity of the first-order guided wave converges to approximately $0.81 c_{2p}$, while all higher-order guided waves converge to c_{2p} . Moreover, the thicker seawater layer results in a greater number of guided-wave modes within the same frequency band, enriching the wave behavior in the system.

As shown in Figs. 5(a) and 6, the attenuation curve of the first-order mode increases monotonically with the frequency, while other higher-order modes exhibit strong frequency-selective characteristics. Hence, modes 2–10 were used to demonstrate the influence of the seawater depth on the attenuation curves. Figure 8 presents the effect of seawater depth on the propagation attenuation of guided waves in a viscoelastic ice–water–sediment–seafloor coupled system at seawater depths of 100, 500, and 1000 m, respectively. The seawater depth has a relatively weak influence on the curve structures of the guided waves in each order.

However, the seawater depth significantly influences the attenuation values and frequency bands of higher-order modes. As the mode order increases, the attenuation peak value of each mode attenuation increases and changes almost linearly with the mode order. In addition, a thicker seawater layer leads to a greater number of guided-wave modes within the same frequency band, further enriching the propagation characteristics of the system. As shown in Fig. 8, the frequency band of peak values was between 0 and 80, 0 and 18, and 0 and 10 Hz for the 100, 500, and 1000 m seawater depths, respectively.

Notably, although no more than 1000 m of seawater depth was used for the numerical simulation, the spectral method developed in this study can also be applied to deeper marine environments without increased complexity or loss of computational efficiency, which is one of the apparent advantages of the spectral method in calculating the dispersion and attenuation curves.

V. CONCLUSION

In this study, the spectral method was used to determine the complex dispersion relation and attenuation of guided waves in a viscoelastic ice–water–sediment–seafloor coupled

system proposed for the Arctic marine environment. Compared to other numerical techniques used to simulate the complex dispersion relation of guided waves in a coupled viscoelastic system, such as the Muller method (Muller, 1956) and the minimum peak method (Lowe, 1995; Barshinger and Rose, 2004), the spectral method demonstrated advantages in terms of efficiency, numerical accuracy, and code simplicity. In addition, when compared to the finite difference method used in the Kraken program (Porter and Reiss, 1984, 1985), the spectral method exhibited a higher order of convergence and avoided the Runge phenomenon.

The generalized eigenvalue problem for guided-wave propagation in the coupled system was constructed by discretizing the wave equations and boundary conditions, and by using the collocation points and differential matrices. A numerical program was developed to solve the eigenvalue equations. Moreover, the attenuation characteristics of the guided waves were analyzed, with particular focus on the effects of ice thickness, damping property, and seawater depth on the phase-velocity dispersion and attenuation curves. The numerical results showed that the attenuation of the first-order guided wave was significantly greater than that of the higher-order modes and increased monotonically with frequency. The attenuation curves for the higher-order modes (greater than or equal to the second order) displayed a characteristic fluctuation pattern. Compared to ice layer thickness, the damping property of the ice layer had a more pronounced influence on the attenuation of guided waves in the coupled system. Additionally, an increase in seawater depth caused an overall shift in the attenuation curves of the higher-order guided waves to lower frequencies.

Owing to the complexity of theoretical derivation and numerical calculation, the Arctic Ocean was modeled as a four-layer coupled system of ice–seawater–sediment–seafloor in this study. Although the modeling differs from the actual Arctic, the conclusions obtained, such as the coupling mechanism, frequency dispersion, and attenuation characteristics of the guided waves, are still of significant value. In future studies, the spectral method may be extended to address the problem of transient acoustic wave propagation in a viscoelastic ice–water–sediment–seafloor coupled system, specifically by solving the non-homogeneous wave equations. While this presents significant challenges, it is a crucial step toward understanding the influence of acoustic source properties on the excitation of guided waves in a coupled system. Moreover, in addition to environmental characteristics, such as the isotropic property and rough boundary of the ice layer, the acoustic velocity profile can be considered when modeling the waveguide in the Arctic Ocean.

ACKNOWLEDGMENTS

This work was supported by the National Natural Science Foundation of China Grant No. U22A2012, and the Open Fund of State Key Laboratory of Acoustics, Chinese Academy of Sciences Grant Nos. SKLA202101 and SKLA202309. The authors would like to thank Mr. Jianming Wu, Mr. Shenqin Huang, and Dr. Xiaokang Zhang from Xiamen University for their contributions to the discussion of this research.

AUTHOR DECLARATIONS

Conflict of Interest

No potential conflict of interest was reported by the authors.

DATA AVAILABILITY

Data sharing is not applicable to this article as no new data were created or analyzed in this study.

APPENDIX A: CONSTRUCTION AND STRUCTURE OF THE DIFFERENTIAL MATRIX

As shown in Eq. (14), the role of the differential matrix is to convert continuous derivative operation into a discrete-matrix algebraic operation. The following example of Chebyshev–Gauss interpolating with N collocation points on a standard interval $[-1, 1]$ was demonstrated to illustrate the effect and structure of a differential matrix.

The collocation points were generated using Eq. (12): $1 = x_1 > x_2 > \dots > x_N = -1$. A differentiable function f defined on the interval $[-1, 1]$ can be discretized at each collocation point as f_1, f_2, \dots, f_N , respectively. Then, the corresponding Lagrange interpolating function $L_N(x)$ can be formulated as follows:

$$L_N(x) = \sum_{i=1}^N \phi_i(x) f_i, \quad (\text{A1})$$

where the interpolating basis function

$$\phi_i(x) = \prod_{j=1, j \neq i}^N \frac{x - x_j}{x_i - x_j}. \quad (\text{A2})$$

Equations (A1) and (A2) exhibit the equivalent relation that $L_N(x_i) = f_i$; furthermore, let the derivative of $L_N(x)$ be the approximate value of f' , then Eq. (A1) becomes as follows:

$$\begin{pmatrix} f'_1 \\ f'_2 \\ \vdots \\ f'_N \end{pmatrix} = \begin{pmatrix} d_{11} & d_{12} & \cdots & d_{1N} \\ d_{21} & d_{22} & \cdots & d_{2N} \\ \vdots & \vdots & \vdots & \vdots \\ d_{N1} & d_{N2} & \cdots & d_{NN} \end{pmatrix} \begin{pmatrix} f_1 \\ f_2 \\ \vdots \\ f_N \end{pmatrix}, \quad (\text{A3})$$

where the element

$$d_{ij} = \left. \frac{d\phi_i(x)}{dx} \right|_{x=x_j}, \quad i, j = 1, 2, \dots, N. \quad (\text{A4})$$

Since the node x_j in Eq. (A4) was the collocation point defined by Eq. (12), then the matrix formed by d_{ij} can be determined for the given N , which was the differential matrix denoted as \mathbf{D} , indicating the relation between the function and derivative values. Moreover, the element d_{ij} can be explicitly expressed as follows:

$$d_{11} = \frac{2(N-1)^2 + 1}{6}, \quad (\text{A5})$$

$$d_{NN} = -\frac{2(N-1)^2 + 1}{6}, \quad (\text{A6})$$

$$d_{ii} = \frac{-x_i}{2(1-x_i^2)}, \quad i = 2, 3, \dots, N-1, \quad (\text{A7})$$

$$d_{ij} = \frac{\varepsilon_i (-1)^{i+j}}{\varepsilon_j x_i - x_j}, \quad i, j = 1, 2, \dots, N, i \neq j, \quad (\text{A8})$$

where the parameter

$$\varepsilon_i = \begin{cases} 2, & \text{and } i = 1, N, \\ 1, & \text{and } i = 2, 3, \dots, N-1. \end{cases} \quad (\text{A9})$$

APPENDIX B: CONSTRUCTION AND STRUCTURE OF DISCRETIZED DISPLACEMENT AND STRESS MATRIX

According to the constitutive relation (Achenbach, 1975), the relationships between the displacement

components and displacement potentials are given by the following:

$$u_i^x = jk\Phi_i + \frac{d}{dz}\Psi_i, \quad (\text{B1})$$

$$u_i^z = \frac{d}{dz}\Phi_i - jk\Psi_i. \quad (\text{B2})$$

The relationships between the stress components and the displacement potentials are as follows:

$$\sigma_i^{zz} = \left[(\lambda_i + 2\mu_i) \frac{d^2}{dz^2} - \lambda_i k^2 \right] \Phi_i - 2jk\mu_i \frac{d}{dz}\Psi_i, \quad (\text{B3})$$

$$\sigma_i^{xz} = 2jk\mu_i \frac{d}{dz}\Phi_i + \mu_i \left(\frac{d^2}{dz^2} + k^2 \right) \Psi_i. \quad (\text{B4})$$

By discretizing Eqs. (B1) and (B2) at the corresponding collocation points and replacing the derivative operations with differential matrices, the discretized displacement matrix is obtained as follows:

$$\begin{pmatrix} \hat{\mathbf{u}}_1^x \\ \mathbf{u}_1^z \\ \hat{\mathbf{u}}_2^x \\ \mathbf{u}_2^z \\ \hat{\mathbf{u}}_3^x \\ \mathbf{u}_3^z \\ \hat{\mathbf{u}}_4^x \\ \mathbf{u}_4^z \end{pmatrix} = \begin{pmatrix} -k^2 \mathbf{I}_1 & \mathbf{D}_1 & 0 & 0 & 0 & 0 \\ \mathbf{D}_1 & -\mathbf{I}_1 & 0 & 0 & 0 & 0 \\ 0 & 0 & -k^2 \mathbf{I}_2 & 0 & 0 & 0 \\ 0 & 0 & \mathbf{D}_2 & 0 & 0 & 0 \\ 0 & 0 & 0 & -k^2 \mathbf{I}_3 & 0 & 0 \\ 0 & 0 & 0 & \mathbf{D}_3 & 0 & 0 \\ 0 & 0 & 0 & 0 & -k^2 \mathbf{I}_4 & \mathbf{D}_4 \\ 0 & 0 & 0 & 0 & \mathbf{D}_4 & -\mathbf{I}_4 \end{pmatrix} \begin{pmatrix} \Phi_1 \\ \hat{\Psi}_1 \\ \Phi_2 \\ \Phi_3 \\ \Phi_4 \\ \hat{\Psi}_4 \end{pmatrix}, \quad (\text{B5})$$

where $\hat{\mathbf{u}}_i^x = jk\mathbf{u}_i^x$ and $\hat{\Psi}_i = jk\Psi_i$ are adopted for notational convenience. The first matrix on the right-hand side of Eq. (B5) is denoted by \mathbf{U} . Similarly, by discretizing Eqs. (B3) and (B4), the following is obtained for the stress components:

$$\begin{pmatrix} \hat{\sigma}_1^{zz} \\ \hat{\sigma}_1^{xz} \\ \hat{\sigma}_2^{zz} \\ \hat{\sigma}_3^{zz} \\ \hat{\sigma}_4^{zz} \\ \hat{\sigma}_4^{xz} \end{pmatrix} = \mu_1 \begin{pmatrix} \mathbf{S}_{11} & \mathbf{S}_{12} & 0 & 0 & 0 & 0 \\ \mathbf{S}_{21} & \mathbf{S}_{22} & 0 & 0 & 0 & 0 \\ 0 & 0 & \mathbf{S}_{33} & 0 & 0 & 0 \\ 0 & 0 & 0 & \mathbf{S}_{44} & 0 & 0 \\ 0 & 0 & 0 & 0 & \mathbf{S}_{55} & \mathbf{S}_{56} \\ 0 & 0 & 0 & 0 & \mathbf{S}_{65} & \mathbf{S}_{66} \end{pmatrix} \begin{pmatrix} \Phi_1 \\ \hat{\Psi}_1 \\ \Phi_2 \\ \Phi_3 \\ \Phi_4 \\ \hat{\Psi}_4 \end{pmatrix}, \quad (\text{B6})$$

where $\hat{\sigma}_i^{xz} = jk\sigma_i^{xz}$. The first matrix on the right-hand side of Eq. (B6) is denoted by \mathbf{S} , with its elements defined as follows:

$$\mathbf{S}_{11} = \frac{(\lambda_1 + 2\mu_1)}{\mu_1} \mathbf{D}_1^2 - \frac{\lambda_1}{\mu_1} k^2 \mathbf{I}_1, \quad (\text{B7})$$

$$\mathbf{S}_{12} = -2\mathbf{D}_1, \quad (\text{B8})$$

$$\mathbf{S}_{21} = -2k^2 \mathbf{D}_1, \quad (\text{B9})$$

$$\mathbf{S}_{22} = \mathbf{D}_1^2 + k^2 \mathbf{I}_1, \quad (\text{B10})$$

$$\mathbf{S}_{33} = \frac{\lambda_2}{\mu_1} (\mathbf{D}_2^2 - k^2 \mathbf{I}_2), \quad (\text{B11})$$

TABLE I. Regularities of embedding boundary conditions to construct operator $\tilde{\mathbf{L}}$.

Boundary condition	Row index of operator \mathbf{L}	Embedding regularity
$\sigma_1^{zz}(x, -h_1) = 0$	1	$\mathbf{S}(N_1, :)$
$\sigma_1^{xz}(x, -h_1) = 0$	N_1	$\mathbf{S}(2N_1, :)$
$u_1^z(x, 0) = u_2^z(x, 0)$	$N_1 + 1$	$\mathbf{U}(N_1 + 1, :) - \mathbf{U}(2N_1 + 2N_2, :)$
$\sigma_1^{zz}(x, 0) = \sigma_2^{zz}(x, 0)$	$2N_1$	$\mathbf{S}(1, :) - \mathbf{S}(2N_1 + N_2, :)$
$\sigma_1^{xz}(x, 0) = 0$	$2N_1 + 1$	$\mathbf{S}(N_1 + 1, :)$
$u_2^z(x, h_2) = u_3^z(x, h_2)$	$2N_1 + N_2$	$\mathbf{U}(2N_1 + N_2 + 1, :) - \mathbf{U}(2N_1 + 2N_2 + 2N_3, :)$
$\sigma_2^{zz}(x, h_2) = \sigma_3^{zz}(x, h_2)$	$2N_1 + N_2 + 1$	$\mathbf{S}(2N_1 + 1, :) - \mathbf{S}(2N_1 + N_2 + N_3, :)$
$u_3^z(x, h_2 + h_3) = u_4^z(x, h_2 + h_3)$	$2N_1 + N_2 + N_3$	$\mathbf{U}(2N_1 + 2N_2 + N_3 + 1, :) - \mathbf{U}(2N_1 + 2N_2 + 2N_3 + N_4 + 1, :)$
$\sigma_3^{zz}(x, h_2 + h_3) = \sigma_4^{zz}(x, h_2 + h_3)$	$2N_1 + N_2 + N_3 + 1$	$\mathbf{S}(2N_1 + N_2 + 1, :) - \mathbf{S}(2N_1 + N_2 + N_3 + 1, :)$
$\sigma_4^{xz}(x, h_2 + h_3) = 0$	$2N_1 + N_2 + N_3 + N_4$	$\mathbf{S}(2N_1 + N_2 + N_3 + N_4 + 1, :)$
$\phi_4(+\infty) = 0$	$2N_1 + N_2 + N_3 + N_4 + 1$	$\mathbf{L}(2N_1 + N_2 + N_3 + N_4, 2N_1 + N_2 + N_3 + N_4) = 1$
$\psi_4(+\infty) = 0$	$2N_1 + N_2 + N_3 + 2N_4$	$\mathbf{L}(2N_1 + N_2 + N_3 + 2N_4, 2N_1 + N_2 + N_3 + 2N_4) = 1$

$$\mathbf{S}_{44} = \frac{\lambda_3}{\mu_1} (\mathbf{D}_3^2 - k^2 \mathbf{I}_3), \quad (\text{B12})$$

$$\mathbf{S}_{55} = \frac{(\lambda_4 + 2\mu_4)}{\mu_1} \mathbf{D}_4^2 - \frac{\lambda_4}{\mu_1} k^2 \mathbf{I}_4, \quad (\text{B13})$$

$$\mathbf{S}_{56} = -2\mathbf{D}_4, \quad (\text{B14})$$

$$\mathbf{S}_{65} = -2k^2 \mathbf{D}_4, \quad (\text{B15})$$

$$\mathbf{S}_{66} = \mathbf{D}_4^2 + k^2 \mathbf{I}_4. \quad (\text{B16})$$

It should be noted that the second Lamé constant μ_1 is used for normalization to improve numerical stability.

APPENDIX C: REGULARITY OF EMBEDDING BOUNDARY CONDITIONS INTO OPERATOR

The sizes of the discretized displacement and stress matrices were $(2N_1 + 2N_2 + 2N_3 + 2N_4) \times (2N_1 + N_2 + N_3 + 2N_4)$ and $(2N_1 + N_2 + N_3 + 2N_4) \times (2N_1 + N_2 + N_3 + 2N_4)$, respectively. The size of the matrix operator \mathbf{L} in Eq. (19) was $(2N_1 + N_2 + N_3 + 2N_4) \times (2N_1 + N_2 + N_3 + 2N_4)$. To embed the boundary conditions from Eqs. (7)–(11), the embedding regularities are provided in Table I.

At the same time, the rows of matrix \mathbf{M} in Eq. (19) corresponding to the row indices of operator \mathbf{L} must be set to zero to satisfy the homogeneous boundary conditions.

Achenbach, J. D. (1975). *Wave Propagation in Elastic Solids* (Elsevier, North-Holland), pp. 66–68.

Adamou, A. T. I., and Craster, R. V. (2004). “Spectral methods for modeling guided waves in elastic media,” *J. Acoust. Soc. Am.* **116**(3), 1524–1535.

Alexander, P., Duncan, A., Bose, N., and Williams, G. (2016). “Modelling acoustic propagation beneath Antarctic sea ice using measured environmental parameters,” *Deep-Sea Res. II Top. Stud. Oceanogr.* **131**, 84–95.

Ananiev, R. A., Dmitrevsky, N. N., Roslyakov, A. G., Chernykh, D. V., Moroz, E. A., Zarayskaya, Y. A., and Semileto, I. P. (2022). “Acoustic monitoring of gas emission process in the Arctic shelf seas,” *Oceanology* **62**(1), 127–132, <https://doi.org/10.1134/S0001437022010015>.

Åström, J. A., and Benn, D. I. (2019). “Effective rheology across the fragmentation transition for sea ice and ice shelves,” *Geophys. Res. Lett.* **46**(22), 13099–13106, <https://doi.org/10.1029/2019GL084896>.

Baggeroer, A. B., and Collis, J. M. (2022). “Transmission loss for the Beaufort Lens and the critical frequency for mode propagation during ICEX-18,” *J. Acoust. Soc. Am.* **151**(4), 2760–2772.

Barclay, D. R., Martin, B. S., Hines, P. C., Hamilton, J. M., Zykov, M., Deveau, T., and Borys, P. (2023). “Observed transmissions and ocean-ice-acoustic coupled modeling in the Beaufort Sea,” *J. Acoust. Soc. Am.* **154**(1), 28–47.

Barshinger, J. N., and Rose, J. L. (2004). “Guided wave propagation in an elastic hollow cylinder coated with a viscoelastic material,” *IEEE Trans. Ultrason. Ferroelect. Freq. Contr.* **51**(11), 1547–1556.

Canuto, C., Hussaini, M. Y., Quarteroni, A., and Zang, T. A. (2007). *Spectral Methods: Evolution to Complex Geometries and Applications to Fluid Dynamics* (Springer-Verlag, Berlin).

Carcione, J. M., Herman, G. C., and ten Kroode, A. P. E. (2002). “Seismic modeling,” *Geophysics* **67**(4), 1304–1325.

Chen, W., Hu, S., Wang, Y., Yin, J., Korochensev, V. I., and Zhang, Y. (2021). “Study on acoustic reflection characteristics of layered sea ice based on boundary condition method,” *Waves Random Complex Media* **31**(6), 2177–2196.

Cheng, S., Rogers, W. E., Thomson, J., Smith, M., Doble, M. J., Wadhams, P., Kohout, A. L., Lund, B., Persson, O. P. G., Collins, C. O. III, Ackley, S. F., Montiel, F., and Shen, H. H. (2017). “Calibrating a viscoelastic sea ice model for wave propagation in the Arctic fall marginal ice zone,” *J. Geophys. Res.* **122**(11), 8770–8793, <https://doi.org/10.1002/2017JC013275>.

Choi, Y., Kang, S. G., Jin, Y. K., Hong, J. K., Shin, S. R., Kim, S., and Choi, Y. (2022). “Estimation of the gas hydrate saturation from multi-channel seismic data on the western continental margin of the Chukchi Rise in Arctic Ocean,” *Front. Earth Sci.* **10**, 1025110.

Collins, M. D. (2015). “Treatment of ice cover and other thin elastic layers with the parabolic equation method,” *J. Acoust. Soc. Am.* **137**(3), 1557–1563.

Collins, M. D., Turgut, A., Menis, R., and Schindall, J. A. (2019). “Acoustic recordings and modeling under seasonally varying sea ice,” *Sci. Rep.* **9**(1), 1–11.

Collis, J. M., Frank, S. D., and Metzler, A. M. (2016). “Elastic parabolic equation and normal mode solutions for seismo-acoustic propagation in underwater environments with ice covers,” *J. Acoust. Soc. Am.* **139**(5), 2672–2682.

Epperson, J. F. (1987). “On the Runge example,” *Am. Math. Mon.* **94**(4), 329–341.

Eringen, A. C., and Suhubi, E. S. (1975). *Elastodynamics* (Academic, New York), Vol. II, pp. 437–442.

Fornberg, B. (1975). “On a Fourier method for the integration of hyperbolic equations,” *SIAM J. Numer. Anal.* **12**(4), 509–528.

Fornberg, B. (1998). *A Practical Guide to Pseudospectral Methods* (Cambridge University Press, London).

Funaro, D. (2008). *Polynomial Approximation of Differential Equations* (Springer-Verlag, Berlin).

Gavrilov, A. N., and Mikhalevsky, P. N. (2006). “Low-frequency acoustic propagation loss in the Arctic Ocean: Results of the Arctic climate

- observations using underwater sound experiment," *J. Acoust. Soc. Am.* **119**(6), 3694–3706.
- Gridin, D., Craster, R. V., Fong, J., Lowe, M. J. S., and Beard, M. (2003). "The high-frequency asymptotic analysis of guided waves in a circular elastic annulus," *Wave Motion* **38**(1), 67–90.
- Haas, C., Hendricks, S., Eicken, H., and Herber, A. (2010). "Synoptic airborne thickness surveys reveal state of Arctic sea ice cover," *Geophys. Res. Lett.* **37**(9), L09501, <https://doi.org/10.1029/2010GL042652>.
- Hesthaven, J. S., Gottlieb, S., and Gottlieb, D. (2007). *Spectral Methods for Time-Dependent Problems* (Cambridge University Press, Cambridge), Vol. 21.
- Hope, G., Sagen, H., Storheim, E., Hobaek, H., and Freitag, L. (2017). "Measured and modeled acoustic propagation underneath the rough Arctic sea-ice," *J. Acoust. Soc. Am.* **142**(3), 1619–1633.
- Jensen, F. B., Kuperman, W. A., Porter, M. B., and Schmidt, H. (2011). *Computational Ocean Acoustics* (Springer, New York).
- Jokat, W., Weigelt, E., Kristoffersen, Y., Rasmussen, T., and Schöne, T. (1995). "New geophysical results from the south-western Eurasian Basin (Morris Jesup Rise, Gakkel Ridge, Yermak Plateau) and the Fram Strait," *Geophys. J. Int.* **123**(2), 601–610.
- Karpfinger, F., Gurevich, B., and Bakulin, A. (2008a). "Modeling of wave dispersion along cylindrical structures using the spectral method," *J. Acoust. Soc. Am.* **124**(2), 859–865.
- Karpfinger, F., Gurevich, B., and Bakulin, A. (2008b). "Modeling of axisymmetric wave modes in a poroelastic cylinder using spectral method," *J. Acoust. Soc. Am.* **124**(4), EL230–EL235.
- Karpfinger, F., Valero, H. P., Gurevich, B., Bakulin, A., and Sinha, B. (2010). "Spectral-method algorithm for modeling dispersion of acoustic modes in elastic cylindrical structures," *Geophysics* **75**(3), H19–H27.
- Laible, H. A., and Rajan, S. D. (1996). "Temporal evolution of under ice reflectivity," *J. Acoust. Soc. Am.* **99**(2), 851–865.
- Lepage, K., and Schmidt, H. (1994). "Modeling of low-frequency transmission loss in the central Arctic," *J. Acoust. Soc. Am.* **96**(3), 1783–1795.
- Li, J., Mondal, S., and Shen, H. H. (2015). "Sensitivity analysis of a viscoelastic parameterization for gravity wave dispersion in ice covered seas," *Cold Reg. Sci. Tech.* **120**, 63–75.
- Li, S., Yuan, S., Liu, S., Wen, J., Huang, Q., and Zhang, Z. (2021). "Characteristics of low-frequency acoustic wave propagation in ice-covered shallow water environment," *Appl. Sci.* **11**(17), 7815.
- Liu, G., and Qu, J. (1998). "Guided circumferential waves in a circular annulus," *J. Appl. Mech.* **65**(2), 424–430.
- Liu, S. X., Tang, L. G., and Li, Z. L. (2021). "Propagation of acoustic waves in a coupled ice-water system for the Arctic Ocean," *Chin. J. Acoust.* **40**(3), 329–344.
- Liu, S., Zeng, Q., Tang, L., and Li, Z. (2024). "Dispersion of waves propagating in the ice-covered Arctic Ocean," *Deep-Sea Res. I Oceanogr. Res. Pap.* **208**, 104301.
- Lowe, M. J. S. (1995). "Matrix techniques for modeling ultrasonic waves in multilayered media," *IEEE Trans. Ultrason. Ferroelect. Freq. Contr.* **42**(4), 525–542.
- McCammon, D. F., and McDaniel, S. T. (1985). "The influence of the physical properties of ice on reflectivity," *J. Acoust. Soc. Am.* **77**(2), 499–507.
- Milnazzo, F. A., Zala, C. A., and Brooke, G. H. (1997). "Rational square-root approximations for parabolic equation algorithms," *J. Acoust. Soc. Am.* **101**(2), 760–766.
- Moler, C. B., and Stewart, G. W. (1973). "An algorithm for generalized matrix eigenvalue problems," *SIAM J. Numer. Anal.* **10**(2), 241–256.
- Muller, D. E. (1956). "A method for solving algebraic equations using an automatic computer," *Math. Comp.* **10**(56), 208–215.
- Orszag, S. A. (1972). "Comparison of pseudospectral and spectral approximation," *Stud. Appl. Math.* **51**(3), 253–259.
- Pelekaniak, K., Blouin, S., and Green, D. (2021). "Performance analysis of underwater acoustic communications in Barrow Strait," *IEEE J. Oceanic Eng.* **46**(4), 1438–1449.
- Porter, M., and Reiss, E. L. (1984). "A numerical method for ocean-acoustic normal modes," *J. Acoust. Soc. Am.* **76**(1), 244–252.
- Porter, M., and Reiss, E. L. (1985). "A numerical method for bottom interacting ocean acoustic normal modes," *J. Acoust. Soc. Am.* **77**(5), 1760–1767.
- Rajan, S. D., Frisk, G. V., Doult, J. A., and Sellers, C. J. (1993). "Determination of compressional wave and shear wave speed profiles in sea ice by crosshole tomography: Theory and experiment," *J. Acoust. Soc. Am.* **93**(2), 721–738.
- Schwarz, J., and Weeks, W. F. (1977). "Engineering properties of sea ice," *J. Glaciol.* **19**(81), 499–531.
- Sinha, B. K., Plona, T. J., Kostek, S., and Chang, S. K. (1992). "Axisymmetric wave propagation in fluid-loaded cylindrical shells. I: Theory," *J. Acoust. Soc. Am.* **92**(2), 1132–1143.
- Shen, J., Tang, T., and Wang, L. L. (2011). *Spectral Methods: Algorithms, Analysis and Applications* (Springer-Verlag, Berlin).
- Stakgold, I., and Holst, M. J. (2011). *Green's Functions and Boundary Value Problems* (Wiley, New York).
- Timco, G. W., and Weeks, W. F. (2010). "A review of the engineering properties of sea ice," *Cold Reg. Sci. Tech.* **60**(2), 107–129.
- Trefethen, L. N. (2000). *Spectral Methods in MATLAB* (Society for Industrial and Applied Mathematics, Philadelphia).
- Valle, C., Qu, J., and Jacobs, L. J. (1999). "Guided circumferential waves in layered cylinders," *Int. J. Eng. Sci.* **37**(11), 1369–1387.
- Wang, R., and Shen, H. H. (2010). "Gravity waves propagating into an ice-covered ocean: A viscoelastic model," *J. Geophys. Res.* **115**, C06024, <https://doi.org/10.1029/2009JC005591>.
- Weideman, J. A., and Reddy, S. C. (2000). "A MATLAB differentiation matrix suite," *ACM Trans. Math. Softw.* **26**(4), 465–519.
- Zeng, Q., Liu, S., Tang, L., and Li, Z. (2024). "Theoretical and numerical study on transient acoustic wave propagation across ice layers in the Arctic Ocean," *J. Acoust. Soc. Am.* **155**(5), 3132–3143.
- Zhang, C., and Zhao, X. (2021). "Theoretical method for calculating the sea ice elastic modulus in an ocean wave model," *Appl. Ocean Res.* **114**, 102800.
- Zharnikov, T. V., Syresin, D. E., and Hsu, C. J. (2013). "Calculating the spectrum of anisotropic waveguides using a spectral method," *J. Acoust. Soc. Am.* **134**(3), 1739–1753.